Chiral Light Design and Detection Inspired by Optical Antenna Theory

*Lisa V. Poulikakos, Prachi Thureja, Alexia Stollmann, Eva De Leo, and David J. Norris**

Optical Materials Engineering Laboratory, Department of Mechanical and Process Engineering,

ETH Zurich, 8092 Zurich, Switzerland

Supporting Information

S1. Derivations of Plane- and Evanescent-Wave Optical Chirality Density

The *optical chirality density*, $\chi = \frac{1}{2}[\mathbf{D} \cdot (\boldsymbol{\nabla} \times \mathbf{E}) + \mathbf{B} \cdot (\boldsymbol{\nabla} \times \mathbf{H})]$, is directly proportional to the asymmetry in the excitation rate of a chiral molecule, where **E**, **D**, **H**, and **B** are the time-dependent electric and magnetic fields.[1] In its time-averaged form, χ becomes:

$$\bar{\chi} = -\frac{\omega}{2}\,\mathrm{Im}(\boldsymbol{\mathcal{D}}^* \cdot \boldsymbol{\mathcal{B}}), \tag{S1}$$

where $\boldsymbol{\mathcal{D}}$ and $\boldsymbol{\mathcal{B}}$ are the complex field amplitudes and ω is the angular frequency. We first derive the optical chirality density for a *z*-propagating plane wave with phase shift ψ, complex electric field amplitude $\boldsymbol{\mathcal{E}}(\mathbf{r}) = \mathcal{E}_0 e^{i\boldsymbol{k}\cdot\boldsymbol{r}}(a, \mathrm{e}^{\mathrm{i}\psi}b, 0)^T$, wavenumber $k = |\boldsymbol{k}| = \sqrt{k_x^2 + k_y^2 + k_z^2}$, vacuum permittivity ε_0, and $|a|^2 + |b|^2 = 1$. The spatial coordinate is denoted by **r**. From Maxwell's equations, the corresponding complex magnetic field amplitude is $\boldsymbol{\mathcal{H}}(\mathbf{r}) = \frac{k}{\mu_0\omega}\mathcal{E}_0 e^{i\boldsymbol{k}\cdot\boldsymbol{r}}(-\mathrm{e}^{\mathrm{i}\psi}b, a, 0)^T$. Inserting this into eq S1 yields:

$$\bar{\chi}_{PW} = ab\varepsilon_0 k|\mathcal{E}_0|^2 \sin(\psi). \tag{S2}$$

Equation S2 reaches its extrema at $\bar{\chi}_{CPL} = \pm(\varepsilon_0 k|\mathcal{E}_0|^2)/2$ for circularly polarized light with $a = b = \frac{\sqrt{2}}{2}$ and $\psi = \frac{(2n+1)\pi}{2}$ for integers *n*.

Next, we derive the optical chirality density for a *z*-decaying evanescent wave with $\boldsymbol{\mathcal{E}}(\mathbf{r}) = (\mathcal{E}_x, \mathcal{E}_y, \mathcal{E}_z)^T e^{\pm i\boldsymbol{k}\cdot\boldsymbol{r}}$ and $k_x^2 + k_y^2 > k^2$. From Maxwell's equations, the corresponding complex magnetic field amplitude is:

$$\boldsymbol{\mathcal{H}}(\mathbf{r}) = \frac{-ie^{\pm i\boldsymbol{k}\cdot\boldsymbol{r}}}{\mu_0\omega}\begin{pmatrix} ik_y\mathcal{E}_z + k_z\mathcal{E}_y \\ -k_z\mathcal{E}_x - ik_x\mathcal{E}_z \\ ik_x\mathcal{E}_y - ik_y\mathcal{E}_x \end{pmatrix}. \tag{S3}$$

Using Euler's formula, we write the complex electric field amplitude as: $\boldsymbol{\mathcal{E}}(\mathbf{r}) = (|\mathcal{E}_x|e^{i\psi_x}, |\mathcal{E}_y|e^{i\psi_y}, |\mathcal{E}_z|e^{i\psi_z})^T e^{\pm i\boldsymbol{k}\cdot\boldsymbol{r}}$, where ψ_m is the phase shift along the *m*-axis with $m \in [x, y, z]$. Inserting this into eq S1 yields:

$$\bar{\chi}_{ev} = \pm\varepsilon_0|\mathcal{E}_z|\big(|\mathcal{E}_x|k_y \sin(\varphi_x - \varphi_z) - |\mathcal{E}_y|k_x \sin(\varphi_y - \varphi_z)\big). \tag{S4}$$

Equation S4 reaches its extrema for one of two cases:

$$\begin{cases} (i) \;\; \varphi_x - \varphi_z = \frac{(4n+1)\pi}{2} \;\text{ and }\; \varphi_y - \varphi_z = \frac{(4n+3)\pi}{2} \\ (ii) \;\; \varphi_x - \varphi_z = \frac{(4n+3)\pi}{2} \;\text{ and }\; \varphi_y - \varphi_z = \frac{(4n+1)\pi}{2} \end{cases} \tag{S5}$$

for integers *n*. This results in the maximum optical chirality density:

$$\bar{\chi}_{max,ev} = \pm\varepsilon_0|\mathcal{E}_z|\big(|\mathcal{E}_x|k_y + |\mathcal{E}_y|k_x\big), \tag{S6}$$

which can exceed $\bar{\chi}_{\mathrm{CPL}}$ as k_x and k_y are theoretically unlimited for evanescent waves.

S2. Conservation Law of Optical Chirality in Lossy, Dispersive Media

Optical chirality follows a conservation law analogous to Poynting's theorem.[1,2] For systems where light interacts with matter, the conservation law of optical chirality in lossy, dispersive media was previously introduced[3] and the results are summarized in this section.

In source-free systems for time-harmonic fields, the conservation law of optical chirality in lossy, dispersive media is written as:

$$-2\omega \int_V \mathrm{Im}(\chi_e - \chi_m)\mathrm{d}^3\mathrm{x} + \int_S \mathrm{Re}(\boldsymbol{\mathcal{F}} \cdot \mathbf{n})\mathrm{d}^2\mathrm{x} = 0, \tag{S7}$$

where the first term represents optical chirality dissipation and the second optical chirality flux, and $\boldsymbol{\mathcal{E}}$ and $\boldsymbol{\mathcal{H}}$ are complex field amplitudes. For the optical chirality dissipation, $\mathrm{Im}(\chi_e - \chi_m) = \frac{1}{8}[-\nabla\epsilon' \cdot \mathrm{Im}(\boldsymbol{\mathcal{E}} \times \boldsymbol{\mathcal{E}}^*) - \nabla\mu' \cdot \mathrm{Im}(\boldsymbol{\mathcal{H}} \times \boldsymbol{\mathcal{H}}^*)] + \frac{1}{4}\omega(\epsilon'\mu'' + \epsilon''\mu')\mathrm{Im}(\boldsymbol{\mathcal{E}}^* \cdot \boldsymbol{\mathcal{H}})$, where in piecewise homogeneous, isotropic media, the first term is non-zero at interfaces.[3,4]

The optical chirality flux is defined as $\boldsymbol{\mathcal{F}} = \frac{1}{4}[\boldsymbol{\mathcal{E}} \times (\nabla \times \boldsymbol{\mathcal{H}}^*) - \boldsymbol{\mathcal{H}}^* \times (\nabla \times \boldsymbol{\mathcal{E}})]$, with $\epsilon = \epsilon' + \mathrm{i}\epsilon''$ as the complex electric permittivity and $\mu = \mu' + \mathrm{i}\mu''$ as the complex magnetic permeability. In the far field, where our measurement takes place, $\boldsymbol{\mathcal{F}}$ can be approximated as the weighted superposition of left- and right-handed circularly polarized plane waves.[5] Thus, the far-field (FF) optical chirality flux becomes: $\boldsymbol{\mathcal{F}}_{\boldsymbol{FF}} = |l|^2\boldsymbol{\mathcal{F}}_{\boldsymbol{LCPL}} + |r|^2\boldsymbol{\mathcal{F}}_{\boldsymbol{RCPL}}$, where $\boldsymbol{\mathcal{F}}_{\boldsymbol{LCPL}}$ and $\boldsymbol{\mathcal{F}}_{\boldsymbol{RCPL}}$ are the optical chirality flux of a left- (LCPL) and right-handed (RCPL) circularly polarized plane wave with weighting factors *l* and *r* for left- and right-handed circular polarization respectively. Thus, $\boldsymbol{\mathcal{F}}$ becomes directly proportional to the third Stokes parameter:[3]

$$\boldsymbol{\mathcal{F}}_{\boldsymbol{FF}} = \frac{\omega}{c}(|l|^2\boldsymbol{\mathcal{S}}_{\boldsymbol{LCPL}} - |r|^2\boldsymbol{\mathcal{S}}_{\boldsymbol{RCPL}}), \tag{S8}$$

where $\boldsymbol{S}$ is the Poynting vector.

S3. Derivation of Dipolar Chiral Antenna Parameters

The analytical calculations which model our system are based on the general model of a chiral dipole with electric- and magnetic-dipole moments $\mathbf{p}, \mathbf{m}$, respectively, and polarizability tensor $\boldsymbol{\alpha}$:[6,7]

$$\begin{pmatrix} \mathbf{p} \\ \mathbf{m} \end{pmatrix} = \begin{pmatrix} \alpha_e & i\alpha_c \\ -i\alpha_c^T & \alpha_h \end{pmatrix} \begin{pmatrix} \boldsymbol{\mathcal{E}} \\ \boldsymbol{\mathcal{H}} \end{pmatrix}, \tag{S9}$$

where α_e, the electric polarizability, is dominant and α_h, the magnetic polarizability, is negligible for the optical response studied here.[8] Chiroptical properties are attributed to α_c, the magnetoelectric polarizability.[9] Because here we study 2D chiral coupled metallic nanoantennas, α_c is induced by the coupling between the nanoantennas leading to $\mathbf{m} \approx 0$. Using subscripts "inc" and "scat" for incident and scattered fields, respectively, we represent a chiral metallic nanoantenna in the quasi-static electric-dipole limit with $\mathbf{p} = \alpha_e \boldsymbol{\mathcal{E}}_{\mathbf{inc}} + i\alpha_c \boldsymbol{\mathcal{H}}_{\mathbf{inc}}$. Assuming an incident *x*-polarized plane wave propagating in +z with $k = k_z$ (axes as in Figure 1 of the main text)**,** the complex field amplitudes are

$$\boldsymbol{\mathcal{E}}_{\boldsymbol{inc}} = \mathcal{E}_0 e^{ikz}(1,0,0), \tag{S10}$$

$$\boldsymbol{\mathcal{E}}_{\boldsymbol{d}} = \boldsymbol{\mathcal{E}}_{\boldsymbol{inc}} + \boldsymbol{\mathcal{E}}_{\boldsymbol{scat}} = (4\pi\epsilon_0 r^3)^{-1}[3\mathbf{n}(\mathbf{n}\cdot\mathbf{p}) - \mathbf{p}], \tag{S11}$$

and $\boldsymbol{\mathcal{H}}_{\mathbf{d}} \approx \boldsymbol{\mathcal{H}}_{\mathbf{inc}}$**.** Resembling the nanorod dimer system studied here, $\mathbf{n} = [0,0,1]^T$ is chosen as the unit vector along the direction of propagation.

S3a. Dipolar Chirality Flux Efficiency

To derive the expression for $\eta_{\bar{\mathcal{F}},d}$ in the main text (eq 9), we determine the optical chirality flux $\boldsymbol{\mathcal{F}} = \frac{1}{4}[\boldsymbol{\mathcal{E}} \times (\nabla \times \boldsymbol{\mathcal{H}}^*) - \boldsymbol{\mathcal{H}}^* \times (\nabla \times \boldsymbol{\mathcal{E}})]$ for the dipolar field quantities $\boldsymbol{\mathcal{E}_d}$ and $\boldsymbol{\mathcal{H}_d}$ defined above:

$$\boldsymbol{\mathcal{F}_d} = \frac{3}{16}\frac{k|\mathcal{E}_0|^2}{\pi}\frac{1}{\epsilon_0\mu_0\omega}\begin{pmatrix} \frac{rcos\theta}{(r^2+\zeta^2)^{\frac{5}{2}}}(-\alpha_c\frac{ik}{\mu_0\omega}cos\theta + \alpha_e sin\theta) \\ \frac{rsin\theta}{(r^2+\zeta^2)^{\frac{5}{2}}}(\alpha_c\frac{ik}{\mu_0\omega}cos\theta - \alpha_e sin\theta) \\ \frac{-\zeta+ik(r^2+\zeta^2)}{(r^2+\zeta^2)^{5/2}}\alpha_c\frac{ik}{\mu_0\omega} \end{pmatrix}, \tag{S12}$$

where (r, θ, ζ) are the radial, polar, and longitudinal cylindrical coordinates. The flux integral $\bar{\mathcal{F}}_d = \int_S \mathrm{Re}(\boldsymbol{\mathcal{F}_d} \cdot \mathbf{n})\mathrm{d}^2\mathrm{x}$ across the longitudinal cylindrical plane at ζ (in the forward direction, $\mathbf{n} = [0,0,1]^{\mathrm{T}}$), comparable to our measurement, then results in:

$$\bar{\mathcal{F}}_d = \frac{3}{16}\frac{|\mathcal{E}_0|^2}{\pi}\frac{k^2}{\epsilon_0\mu_0^2\omega^2}\frac{\theta}{3}\left[-\frac{\zeta}{(r^2+\zeta^2)^{\frac{3}{2}}}\mathrm{Im}(\alpha_c) + \frac{3k}{(r^2+\zeta^2)^{\frac{1}{2}}}\mathrm{Re}(\alpha_c)\right], \tag{S13}$$

where the first term in eq S13 ($\propto \frac{1}{\zeta^2}$) becomes negligible for large ζ in the far field.

After inserting integration boundaries for $\theta \in [0,2\pi]$ we obtain:

$$\bar{\mathcal{F}}_d \approx \mathrm{Re}(\alpha_c)\frac{3}{8}\frac{\omega}{\mu_0 c}\frac{|\mathcal{E}_0|^2}{\sqrt{r^2+\zeta^2}} \tag{S14}$$

which leads to the expression for $\eta_{\bar{\mathcal{F}},d}$ in eq 9 of the main text, since $\eta_{\bar{\mathcal{F}},d} \coloneqq \frac{c}{\omega P_{tot}}\bar{\mathcal{F}}_d$.

S3b. Dipolar Chiral Antenna Aperture

We now derive the expression for $\sigma_{\bar{X},d}$ (eq 10 in the main text). For a point dipole at the origin **0**, the optical chirality dissipation can be written as:

$$\bar{X} = 2\omega \int_V \mathrm{Im}(\chi_e - \chi_m)\delta(\boldsymbol{x})\mathrm{d}^3\mathrm{x} \tag{S15}$$

where $\delta(\boldsymbol{x})$ is the Dirac delta function. In the limit of a point dipole, the first term on the right-hand side of eq 8 in the main text becomes negligible for the spatially constant material functions studied here. Therefore, we have:

$$\mathrm{Im}(\chi_e - \chi_m) = \frac{1}{4}\omega(\epsilon'\mu'' + \epsilon''\mu')\mathrm{Im}(\boldsymbol{\mathcal{E}}_{\mathbf{d,in}}{}^{*} \cdot \boldsymbol{\mathcal{H}}_{\mathbf{d,in}}), \tag{S16}$$

where $\boldsymbol{\mathcal{E}}_{\mathbf{d,in}}$ and $\boldsymbol{\mathcal{H}}_{\mathbf{d,in}}$ are the fields inside the dipole. The dipole moment causes a polarization field $\boldsymbol{\mathcal{P}} = \alpha_e\boldsymbol{\mathcal{E}}_{\mathbf{inc}} + i\alpha_c\boldsymbol{\mathcal{H}}_{\mathbf{inc}}$, where "inc" denotes the incident fields. This leads to an electric field within the dipole described by: $\boldsymbol{\mathcal{E}}_{\mathbf{d,in}} = \frac{\boldsymbol{\mathcal{P}}}{(\epsilon' + i\epsilon'' - \epsilon_0)}$. Further, the magnetic field remains $\boldsymbol{\mathcal{H}}_{\mathbf{d,in}} \approx \boldsymbol{\mathcal{H}}_{\mathbf{inc}}$ and we can set $\mu'' = 0$. Thus, we obtain:

$$\bar{X}_d = -[(\epsilon' - \epsilon_0)\mathrm{Re}(\alpha_c) + \epsilon'' Im(\alpha_c)]\frac{1}{2}\frac{\epsilon''\mu'}{\mu_0^2}\frac{1}{(\epsilon' - \epsilon_0)^2 + \epsilon''^2}k^2|\mathcal{E}_0|^2 \tag{S17}$$

The second term of eq S17 becomes negligible, as $\epsilon'' \ll \epsilon'$ for metals such as silver studied here,[10] leading to: $\bar{X}_d \approx -\mathrm{Re}(\alpha_c)\frac{1}{2}\frac{\epsilon''\mu'}{\mu_0^2}\frac{(\epsilon' - \epsilon_0)}{(\epsilon' - \epsilon_0)^2 + \epsilon''^2}k^2|\mathcal{E}_0|^2$. This results in eq 10 in the main text, since $\sigma_{\bar{X}_d} := \frac{\bar{X}_d}{p_{inc}}$.

S3c. Dipolar Optical Chirality Density

Finally, we derive the expression for $\bar{\chi}_d$ (eq 11 in the main text), which was obtained by inserting the dipolar fields into eq. S1, in free space surrounding the dipole. Because

$$\boldsymbol{\mathcal{E}}_{\mathbf{d}}^{*} \cdot \boldsymbol{\mathcal{H}}_{\boldsymbol{d}} = \frac{k^2|\mathcal{E}_0|^2}{4\pi r^3 \varepsilon_0 \mu_0^2 \omega^2} i\alpha_c^{*}, \tag{S18}$$

we obtain the expression for $\bar{\chi}_d$ given in eq 11 in the main text from $\bar{\chi}_d = -\frac{\omega}{2}\varepsilon_0\mu_0\mathrm{Im}(\boldsymbol{\mathcal{E}}_{\mathbf{d}}^{*} \cdot \boldsymbol{\mathcal{H}}_{\boldsymbol{d}})$.

S4. Sample Fabrication and Characterization

For sample fabrication, Si(100) wafer pieces of 2 × 2 cm size with a 150-nm-thick Si_3N_4 low-pressure chemical vapor deposition mask were patterned. After ultrasonic cleaning in acetone and isopropanol, the substrates were pre-baked for 10 min at 180 °C. Next, ~280 nm of electron-beam resist (Allresist, CSAR 62 AR-P6200) were spin-cast onto each wafer (2000 r.p.m., 60 s), which was subsequently post-baked (180 °C, 5 min). The substrates were then exposed with an electron-beam lithography system (Vistec, EBPG5200) and the resist was subsequently developed (Allresist, AR 600-546). The Si_3N_4 mask was then etched with reactive-ion etching for 8 min (Oxford Instruments, 55 mTorr, 100 W RF, 50 sccm CHF_3, 5 sccm O_2), after which the remaining resist was removed with NMP (Sigma-Aldrich, n-methyl-2-pyrrolidone, 90 min, 130 °C).

The structured wafer was functionalized with a self-assembled monolayer of octadecyltrichlorosilane to decrease adhesion, as previously reported.[11] 50 nm of Ag was then deposited by thermal evaporation (Kurt J. Lesker, Nano36) at 25 Å/s. The Si_3N_4 mask creates a step-edge allowing selective removal of the undesired flat metal with adhsesive tape.[12] Next, the Ag nanostructures were extracted onto a glass microscope slide by template stripping[13] with ultraviolet-light-curable epoxy (Norland 88). The final sample consists of arrays of Ag nanorod antennas on a transparent substrate of glass and epoxy.

Figure S1a,c shows scanning electron micrographs (SEMs) of the right-handed nanorod dimers (R-NRDs, a) and left-handed nanorod dimers (L-NRDs, c) studied here, with a 400 nm scale bar. For SEM imaging, the flat Ag was not removed from the samples, allowing for a conductive substrate to avoid charging and contamination effects in the electron microscope images.

Figure S1b,d shows extinction spectra of the samples taken on an inverted optical microscope (Ti-U, Nikon) with *x*-polarized excitation. The microscope employed an excitation objective ($20\times$, 0.45 numerical aperture, NA) and a collection objective ($10\times$, 0.3 NA).

S5. Chirality Flux Efficiency Experimental Data Analysis

With the experimental setup shown in Figure 2d in the main text, $\eta_{\bar{\mathcal{F}}}$ is detected by extracting the RMS (root mean square) voltage (V_{RMS}) and phase φ from the lock-in amplifier with Labview at each wavelength. As $\eta_{\bar{\mathcal{F}}}$ is directly proportional to the 3rd Stokes parameter (S_3) in the far field (see eq S8), the desired information is obtained from the measurement with:[14]

$$\frac{S_3}{S_0} = \frac{\sqrt{2}\mathrm{V_{RMS}(50\ kHz)}}{J_1[\varphi(50\ \mathrm{kHz})]\mathrm{S_0}}, \tag{S19}$$

where J_1 is the 1st order Bessel function and S_0 is the 0th Stokes parameter. Because this system detects a fully polarized beam, we define S_0 as the total intensity of modulated light at 50 kHz (circularly polarized) and 100 kHz (linearly polarized) with

$$S_0 = \sqrt{2}[V_{RMS}(50\ \mathrm{kHz}) + V_{RMS}(100\ \mathrm{kHz})]. \tag{S20}$$

This leads to:

$$\frac{\bar{\mathcal{F}}}{S_0} = \frac{\mathrm{V_{RMS}(50\ kHz)}}{J_1[\varphi(50\ \mathrm{kHz})][V_{RMS}(50\ \mathrm{kHz})+V_{RMS}(100\ \mathrm{kHz})]}\frac{\omega}{c}. \tag{S21}$$

To compare spectra of samples with different lattice constants, we normalize eq S21 with the maximum value in each sample's extinction spectrum. The extinction is measured as described in Section S4 above. $P_{e,max,norm}$ is flat-field normalized power (unit 1) resulting in the experimental expression for $\eta_{\bar{\mathcal{F}}}$:

$$\eta_{\bar{\mathcal{F}},experimental} = \frac{\mathrm{V_{RMS}(50\ kHz)}}{J_1[\varphi(50\ \mathrm{kHz})][V_{RMS}(50\ kHz)+V_{RMS}(100\ kHz)]} \frac{1}{P_{e,max,norm}}, \qquad \text{(S22)}$$

where the corresponding background $\eta_{\bar{\mathcal{F}}}$ signal collected from the sample-free substrate is subtracted from the expression in eq S22. The background signal arises from minimal residual birefringence in the optics and is below 1-2% of the incident light. The spectra were recorded with 3-nm spectral resolution.

S6. Circular Dichroism

Circular dichroism (CD) spectra were measured by altering our home-built setup as shown in Figure S2a. For CD measurements, the photoelastic modulator (PEM, Hinds Instruments I/FS50) was placed *before* the sample, which leads to alternating excitation with R- and L-CPL in a 50 kHz cycle. Unlike in the $\eta_{\bar{\mathcal{F}}}$ measurement, which analyzes the degree of circular polarization scattered by the sample, in the CD measurement the photomultiplier tube (PMT, Hamamatsu R928) measures the total intensity of the outgoing beam, which is locked into the modulation frequency of the excitation beam.

The inset of Figure S2a shows the principle of CD. As a chiral sample exhibits a different extinction for R- and L-CPL excitation, the intensity of light reaching the detector will vary in amplitude based on the excitation polarization. When this periodic amplitude modulation locks into the PEM electronic signal, the resulting RMS voltage corresponds to the *differential* extinction upon R- and L-CPL excitation. In other words, as the inset shows, the outgoing beam in a CD measurement is elliptical when averaged over a 50 kHz modulation cycle.

The spectral CD data were extracted from the lock-in amplifier with Labview as a root mean square voltage (V_{RMS}) and phase φ, representing the retardation of the modulation in a 50 kHz cycle, and normalized by the direct-current (DC) voltage recorded at 0 kHz. This results in:

$$CD = \frac{V_{RMS}(50\ \mathrm{kHz})\sin[\varphi(50\ \mathrm{kHz})]}{V_{DC}}, \tag{S23}$$

where the corresponding background CD signal, obtained from the sample-free substrate, is subtracted from eq S23.

Figure S2b,c shows the CD spectra of all the R-NRDs (b) and L-NRDs (c) studied here. While CD spectroscopy yields mirror-symmetric spectra for NRDs of opposite handedness, the relationship to chiral evanescent fields cannot be drawn, unlike for $\eta_{\bar{F}}$. Particularly, a comparison of the CD spectra of varying *h* does not show the monotonic behavior seen for $\eta_{\bar{F}}$, which is directly related to the magnetoelectric polarizability and the chiral near fields.

S7. Achiral Control Samples

Several achiral control samples were measured to test our technique. Figure S3a-c shows scanning-electron micrographs for (a) single nanorods, (b) achiral NRDs with *h* = 60 nm, and (c) achiral NRDs with *h* = 80 nm. The scale bar is 400 nm.

Figure S3d,e shows the $\eta_{\bar{F}}$ and CD spectra for the studied achiral control samples, where the vertical-axis scaling corresponds to that in the main text. As expected, the $\eta_{\bar{F}}$ and CD signals are negligible. Particularly, the small signals in the $\eta_{\bar{F}}$ spectra verify that no linear birefringence occurs due to our excitation with *x*-polarized light (axes as in Figure 1 in the main text). The extinction spectra of the control samples are shown in Figure S3f. The maxima of these spectra are used for normalization purposes to compare $\eta_{\bar{F}}$ of different samples.

Finally, Figure S3g shows numerical colormaps of the optical chirality enhancement ($\bar{\chi}/|\bar{\chi}_{CPL}|$) for achiral NRDs with *h* = 60 nm (*z* = 0 plane, NRD center) for various wavelengths

(λ). These maps show equal quantities of positive and negative $\bar{\chi}/|\bar{\chi}_{CPL}|$. Particularly, the achiral coupling does not induce chiral evanescent fields.

S8. Finite-Element Simulations

The numerical computations performed in this work were conducted by the finite-element solver COMSOL Multiphysics 5.2 resulting in time-harmonic, electromagnetic near fields governed by Maxwell's equations. Data from Johnson and Christy[10] were used for the optical material constants of the studied Ag nanostructures. The nanostructures were placed on a dielectric substrate (refractive index $n_{\text{substrate}} = 1.3$) occupying the entire half space below the nanoantenna, with air ($n_{\text{air}} = 1$) occupying the half space above. As the experimental substrate includes a thin air-epoxy layer immediately below the Ag nanoantennas (see Section S4 for sample fabrication), $n_{\text{substrate}}$ is set as an effective refractive index slightly below that of silica glass. Linearly polarized plane-wave excitation (*x*-polarization propagating in +*z*, axes as in Figure 1 in the main text) was performed from a port at the lower domain boundary (*z* = -2250 nm plane).

The computational domain was defined with periodic boundary conditions in *x* and *y* (Floquet periodicity) to replicate the experimentally studied nanoantenna array. As the edge-to-edge distance between outer NRD edges was chosen at 600 nm, the horizontal lattice constant increases with increasing *h* (horizontal nanorod spacing). In the $\pm z$ direction the computational domain is 2250 nm in length, and is bounded by a perfectly matched layer (PML). First, the background fields were computed for a plane wave incident on the substrate (i.e. the Ag nanoantenna was omitted). Next, the scattered fields were obtained by subtracting the background fields from full-field calculations with the Ag nanoantenna.

Far-field spectral data were extracted with 10 nm resolution by surface integration of the *x*-*y* plane at *z* = 2050 nm in COMSOL 5.2. Evaluation at different *z*-values showed convergence to the far field at the chosen *z*-plane with <4% relative numerical error in the relevant wavelength range. The computational $\eta_{\bar{\mathcal{F}}}$ values were obtained with the formula:

$$\eta_{\bar{\mathcal{F}},\,numerical} = \frac{\iint i(\mathcal{E}_x\mathcal{E}_y^* - \mathcal{E}_y\mathcal{E}_x^*)n_z d^2x}{\iint (|\boldsymbol{\mathcal{E}}_x|^2 + |\boldsymbol{\mathcal{E}}_y|^2) d^2x} \frac{1}{P_{e,max,norm}} \tag{S24}$$

which normalizes the third Stokes parameter (proportional to the degree of circular polarization) with $|\boldsymbol{\mathcal{E}}_x|^2 + |\boldsymbol{\mathcal{E}}_y|^2$ (proportional to the far-field intensity of x- and y-polarized light[5]) with $[\eta_{\bar{\mathcal{F}},\,numerical}] = 1$. Furthermore, in accordance with the normalization procedure of the experimental data (see section S5, eq S22), we additionally divide by $P_{e,max,norm}$, the flatfield-normalized maximum value of the average power flow. This is computed as $P_{e,max,norm} = 1 - \frac{P_{trans,min}}{P_{bg}}$, where $P_{trans,min}$ is the minimum transmitted power and P_{bg} is the power of the background fields when no nanostructure is present. As bulk silver material constants are used, where absorption increases at low wavelengths,[10] these values are found in the 400 to 500 nm range. The chiral antenna aperture, $\sigma_{\bar{X}}$, was obtained for the nanorod dimers in COMSOL 5.2 with the conservation law of optical chirality (eq S7).[4] We normalized the optical chirality dissipation by $p_{inc} = \frac{P_{inc}}{V}$, the incident power density evaluated as a surface integral through the z = 2050 nm plane, with *V* as the volume of the two nanorod antennas and we obtain units $[\sigma_{\bar{X},\,numerical}] = \mathrm{m}^2$ for the chiral antenna aperture.

The optical chirality enhancement ($\bar{\chi}/|\bar{\chi}_{CPL}|$) was calculated in MATLAB R2016b by extracting the electric- and magnetic-field data obtained in COMSOL 5.2 with the COMSOL Livelink for MATLAB. Spectral evaluation was performed by data extraction in 10 nm steps at

(0,0,0), which is the center point between nanorods (indicated as * in Figure 2c). Numerical colormaps of $\bar{\chi}/|\bar{\chi}_{CPL}|$ were obtained by data extrapolation onto a 100×100 grid in the $z = 0$ plane, obtained with the MATLAB *meshgrid* function.

A moving average filter (MATLAB *smooth* function) was applied to the spectral data to remove numerical noise. The side-length constraint of the mesh was chosen at 50 nm to achieve a relative numerical discretization error below 1% for the calculated quantities in the significant wavelength range.

S9. Numerical Geometry Optimization

The vertical shift *v* between nanorods (indicated in Figure S4a) was optimized numerically, where positive *v* resulted in R-NRDs and negative *v* resulted in L-NRDs. Figure S4b shows $\eta_{\bar{F}}$ spectra (50 nm spectral steps, raw data) for varying *v* at *h* = 60 nm. A vertical shift *v* = 140 nm is chosen in this work as it yields the largest $\eta_{\bar{F}}$ value for the studied parameter space.

S10. Surface Lattice Resonances

In this section, we discuss the effect of surface lattice resonances. Figure S5a shows numerical $\eta_{\bar{F}}$ spectra extracted at different angles for R-NRD with *h* = 60 nm. As a proof of principle, we consider tilted planes with normal vectors $\boldsymbol{n} = [\sin(\sin^{-1}(\mathrm{NA})), 0, \cos(\sin^{-1}(\mathrm{NA}))]$, where NA corresponds to the numerical aperture of an experimental objective lens. We can compare the $\eta_{\bar{F}}$ spectra for each NA by normalizing with $|\boldsymbol{\mathcal{E}_x}|^2 + |\boldsymbol{\mathcal{E}_y}|^2$ (according to eq S24) through the respective tilted surface. Comparing the spectra for $\mathrm{NA} = 0, 0.3, 0.45$ in Figure S5a (raw data), we find that the effect of the surface lattice resonance at 600 nm becomes more pronounced with increasing NA, as was seen in prior work.[15] Thus, by collecting light numerically in the forward

direction (NA = 0) and experimentally at small angles (NA = 0.3), we minimize the effect of the surface lattice resonances and focus on the optical behavior of single NRDs. In experiment, the surface-lattice-resonance effect is damped due to fabrication imperfections.[15]

Figure S5b shows numerical chiral-antenna-aperture ($\sigma_{\bar{X}}$) spectra for R-NRDs with horizontal shifts h = 60 to 200 nm. Due to chirality conservation, the chiral antenna aperture is related to the optical chirality flux through the entire surface enclosing the studied structure. The surface lattice resonance is dominant for $\sigma_{\bar{X}}$, as the studied NRDs represent a 2D chiral system which scatters an optical chirality flux of opposite sign in forward and backward direction. Thus, the forward and backward components of the optical chirality flux predominantly cancel in the flux integral through a surface enclosing the entire NRD. Further, $\sigma_{\bar{X}}$ demonstrates that the surface lattice resonance exhibits a redshift with increasing $h + p$, where p is defined by the edge-to-edge distance between NRDs (indicated in Figure 2c in the main text). The spectral increase observed for $\sigma_{\bar{X}}$ at low wavelengths can be attributed to silver absorption inherent to the bulk material constants applied in the numerical calculations[10] and a higher order mode of the surface lattice resonance.[16]

S11. Supplemental References

(1) Tang, Y.; Cohen, A. E. *Phys. Rev. Lett.* **2010**, *104* (16), 163901.
(2) Lipkin, D. M. *J. Math. Phys.* **1964**, *5*, 696.
(3) Poulikakos, L. V.; Gutsche, P.; McPeak, K. M.; Burger, S.; Niegemann, J.; Hafner, C.; Norris, D. J. *ACS Photonics* **2016**, *3*, 1619–1625.
(4) Gutsche, P.; Poulikakos, L. V.; Hammerschmidt, M.; Burger, S.; Schmidt, F. *Proc. SPIE 9756, Photonic and Phononic Properties of Engineered Nanostructures VI* **2016**, 97560X.
(5) Novotny, L.; Hecht, B. *Principles of Nano-Optics*, 2nd ed.; Cambridge University Press: Cambridge, 2012.
(6) Sersic, I.; Tuambilangana, C.; Kampfrath, T.; Koenderink, A. F. *Phys. Rev. B* **2011**, *83*, 245102.
(7) Sersic, I.; van de Haar, M. A.; Arango, F. B.; Koenderink, A. F. *Phys. Rev. Lett.* **2012**, *108*, 223903.
(8) Capolino, F. In *Theory and Phenomena of Metamaterials*; Capolino, F., Ed.; CRC Press/Taylor & Francis: Boca Raton, 2009; p II.8-2.

(9) Barron, L. D. *Molecular Light Scattering and Optical Activity*, 2nd ed.; Cambridge University Press: Cambridge, 2009.
(10) Johnson, P. B.; Christy, R. W. *Phys. Rev. B* **1972**, *6*, 4370–4379.
(11) Prins, F.; Kim, D. K.; Cui, J.; De Leo, E.; Spiegel, L. L.; McPeak, K. M.; Norris, D. J. *Nano Lett.* **2017**, *17*, 1319–1325.
(12) McPeak, K. M.; van Engers, C. D.; Blome, M.; Park, J. H.; Burger, S.; Gosálvez, M. A.; Faridi, A.; Ries, Y. R.; Sahu, A.; Norris, D. J. *Nano Lett.* **2014**, *14*, 2934–2940.
(13) Nagpal, P.; Lindquist, N. C.; Oh, S.-H.; Norris, D. J. *Science* **2009**, *325*, 594–597.
(14) Ghosh, N.; Wood, M.; Vitkin, A. In *Handbook of Photonics for Biomedical Science*; Tuchin, V. V., Ed.; CRC Press/Taylor & Francis: Boca Raton, 2010; pp 253–282.
(15) Cotrufo, M.; Osorio, C. I.; Koenderink, A. F. *ACS Nano* **2016**, *10*, 3389–3397.
(16) Wang, D.; Yang, A.; Hryn, A. J.; Schatz, G. C.; Odom, T. W. *ACS Photonics* **2015**, *2*, 1789–1794.

S12. Supplemental Figures

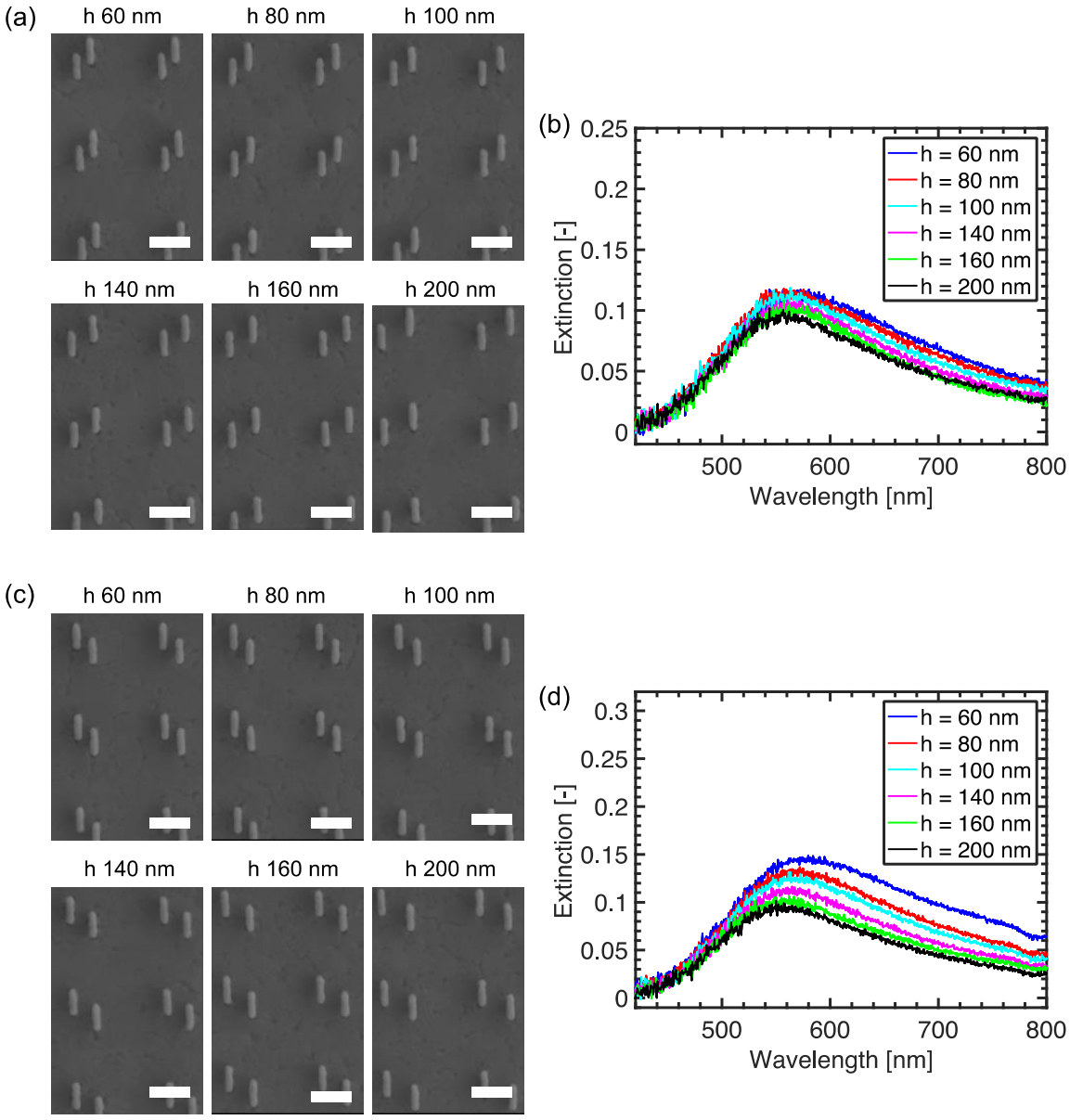

Figure S1. (a) Scanning-electron micrographs of the right-handed nanorod dimers (R-NRDs) with h = 60 to 200 nm. The scale bars are 400 nm. (b) Extinction spectra of the R-NRDs with h = 60 to 200 nm. (c) Scanning-electron micrographs of the left-handed nanorod dimers (L-NRDs) for h = 60 to 200 nm. (d) Extinction spectra of L-NRDs with h = 60 to 200 nm.

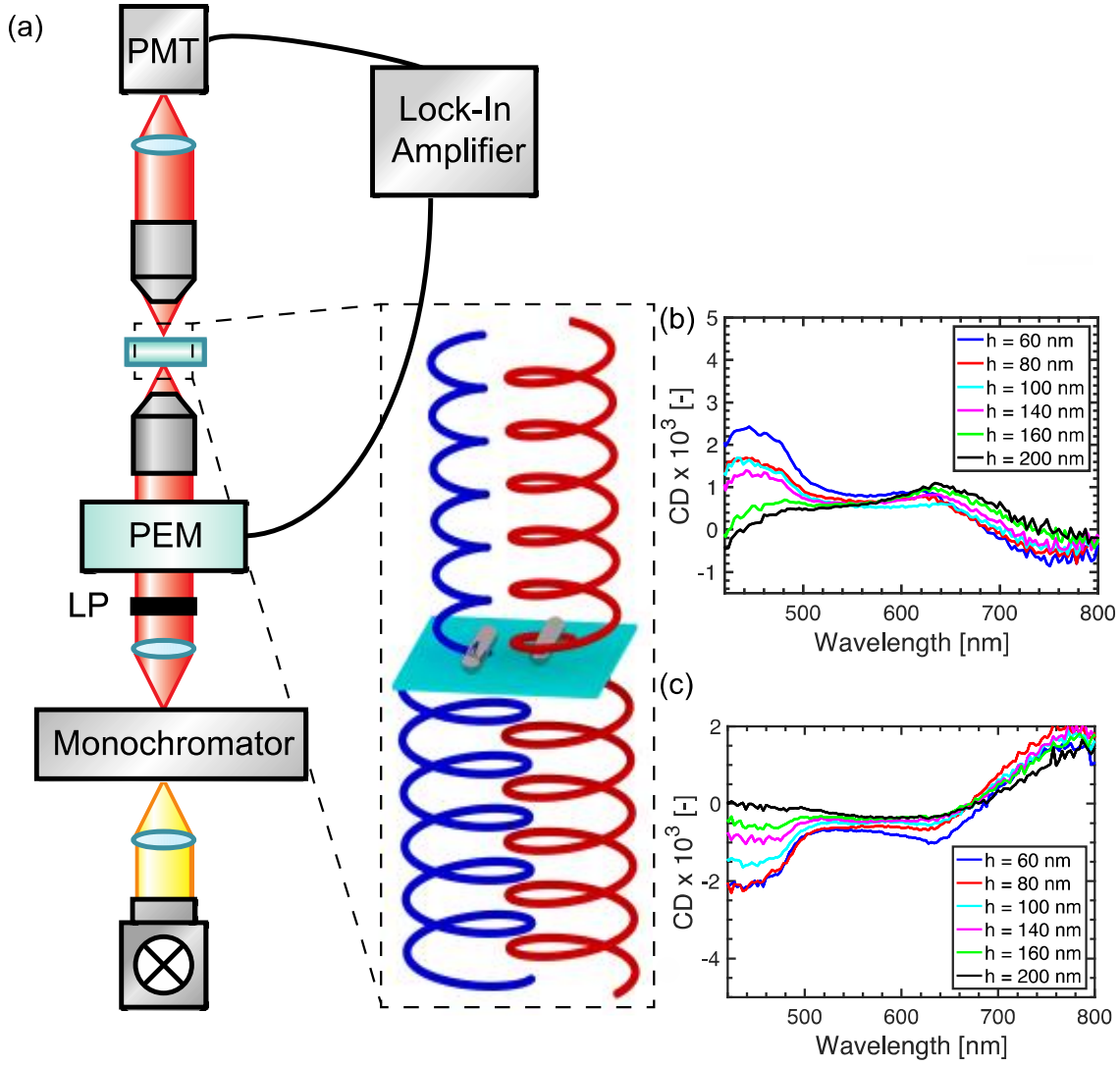

Figure S2. (a) Schematic of the experimental setup modified to measure circular dichroism (CD). Inset: The sample is excited with alternating right- and left-handed circularly polarized light, modulated at 50 kHz by a photoelastic modulator (PEM). The differential extinction of a chiral sample results in an outgoing elliptical beam whose total intensity is measured by a photomultiplier tube (PMT). (b) CD spectra for R-NRDs, h = 60 to 200 nm. (c) CD spectra of L-NRDs, h = 60 to 200 nm.

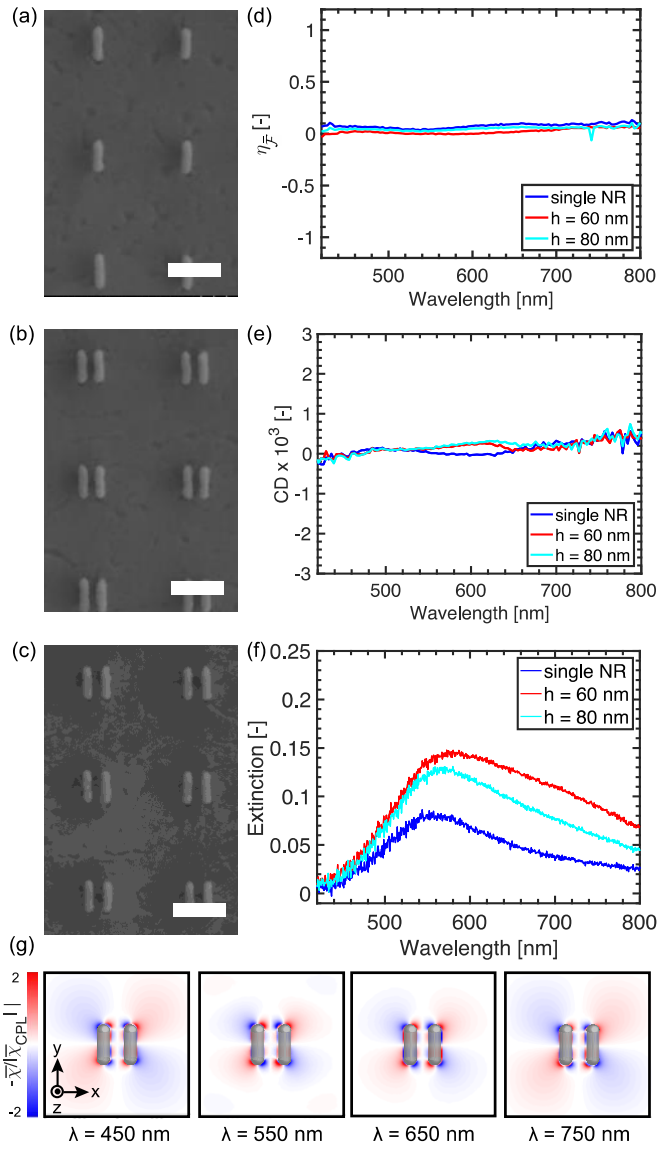

Figure S3. (a-c) Scanning-electron micrographs of achiral control samples with (a) single nanorods, (b) achiral nanorod dimers (NRDs) with h = 60 nm, and (c) achiral NRDs with h = 80 nm. The scale bars are 400 nm. (d) Chirality flux efficiency ($\eta_{\bar{\mathcal{F}}}$) spectra for the achiral control samples shown in (a-c). As expected, achiral samples do not exhibit an $\eta_{\bar{\mathcal{F}}}$ signal. (e) CD spectra for the achiral control samples shown in (a-c). As expected, achiral samples do not exhibit a CD signal. Vertical axis scaling in (d,e) corresponds to that used in the main text. (f) Extinction spectra of the achiral control samples shown in (a-c). (g) Numerical colormaps of the optical chirality enhancement ($\bar{\chi}/|\bar{\chi}_{\mathrm{CPL}}|$) for achiral NRDs with h = 60 nm for various wavelengths (λ). In contrast to chiral NRDs, the coupling in this system does not induce an excess of one handedness of $\bar{\chi}/|\bar{\chi}_{\mathrm{CPL}}|$.

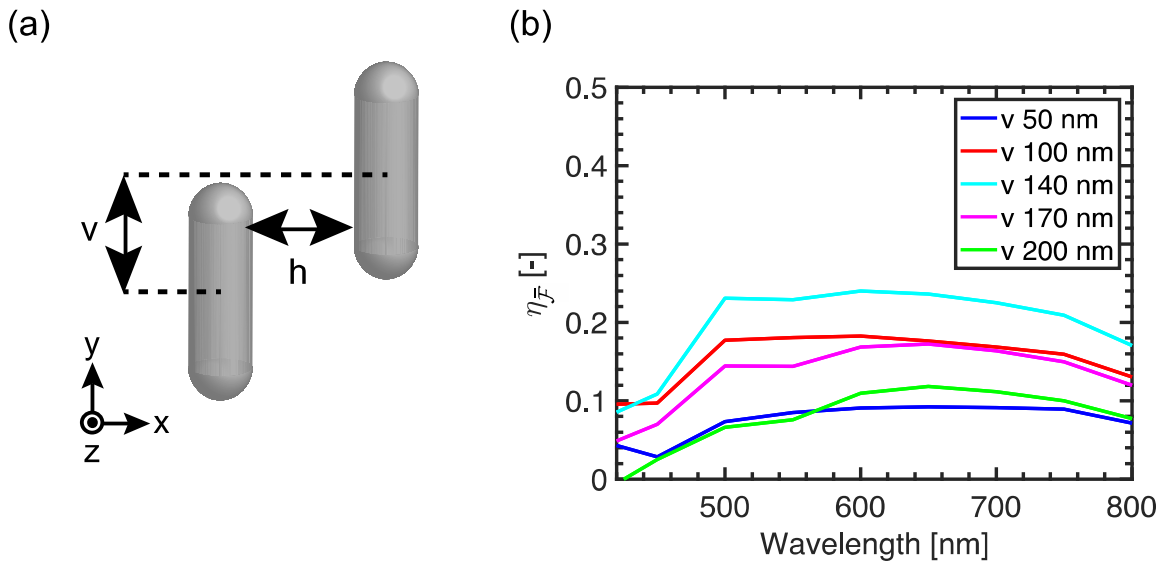

Figure S4. (a) Illustration of the vertical (*v*) and horizontal (*h*) nanorod shift that results in a 2D chiral coupled nanorod dimer (NRD). (b) Simulated $\eta_{\bar{F}}$ spectra for *h* = 60 nm and various *v* with 50 nm wavelength steps. The geometry with *v* = 140 nm is chosen for further investigation in this work.

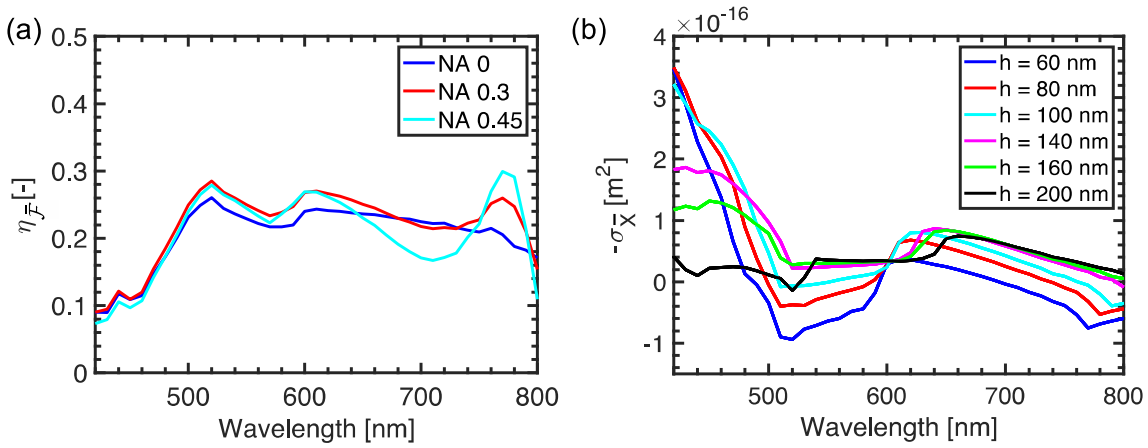

Figure S5. (a) Simulated chirality flux efficiency ($\eta_{\bar{F}}$) spectra evaluated at different angles (tilted planes in real space), representing signal collection with various numerical apertures (NAs). With increasing NA, the surface lattice resonance at 600 nm becomes more prominent. (b) Simulated chiral antenna aperture ($\sigma_{\bar{X}}$) spectra for R-NRDs with horizontal shift h = 60 to 200 nm. The dominant $\sigma_{\bar{X}}$ resonance is determined by the surface lattice resonance, which exhibits a redshift with increasing h, as the distance p defined by the spacing between outer nanorod edges remains constant (see Figure 2c in the main text).